Global Safety Characteristics of Wheeled Mobile Manipulators

6 authors, including:

Nico Mansfeld
Franka Emika GmbH
41 PUBLICATIONS **401** CITATIONS

SEE PROFILE

Mazin Hamad
Chair of Robotics and Systems Intelligence (RSI)
20 PUBLICATIONS **143** CITATIONS

SEE PROFILE

Guillermo Gómez Peña
Technische Universität München
2 PUBLICATIONS **14** CITATIONS

SEE PROFILE

Alexander Kurdas
Technische Universität München
10 PUBLICATIONS **33** CITATIONS

SEE PROFILE

Global Safety Characteristics of Wheeled Mobile Manipulators

Nico Mansfeld[1*], Guillermo Gómez Peña[1,2*], Mazin Hamad[1*],
Alexander Kurdas[1*], Saeed Abdolshah[1] and Sami Haddadin[1]

Abstract—Mobile manipulators have become increasingly popular in industry because they can be used for a large variety of tasks in a versatile and flexible manner. The perception and planning/control schemes of mobile robots enable them to share a workspace with humans. However, as undesired or unforeseen contacts can generally not be avoided, it is essential to understand the intrinsic safety properties of such systems. Then, collision safety can be systematically accounted for in mechanism design, planning, and control. In this paper, we derive the safety characteristics of wheeled mobile manipulators, more specifically the achievable reflected mass and velocity range, and show how they can be related to human injury data in the previously introduced Safety Map for a model-independent and interpretation-free safety assessment. We investigate two common types of wheeled mobile platforms and the combination of these with the seven-DOF Franka Emika robot. We analyze the influence of the vehicle parameters on the safety performance and derive the Safety Map representations for four practically relevant industrial collision scenarios.

Fig. 1: A wheeled mobile manipulator and human co-worker sharing the same workspace[1]. In order to ensure human safety during unwanted collisions, the safety characteristics of the robot must be understood well. This work systematically investigates the safety-relevant dynamic properties of mobile manipulators for practically relevant collision scenarios in industry.

I. INTRODUCTION

In recent years, physical human-robot interaction (pHRI) has become a popular and marketable technology in automation industry. Numerous collaborative robots (also referred to as cobots) such as the Universal Robot family or the KUKA iiwa as well as tactile robots like the Franka Emika robot are commercially available. They enable a high degree of productivity and flexibility in a large variety of tasks. Even more flexibility can be achieved with mobile manipulators that comprise an actuated platform and a (collaborative) robot manipulator. Such systems can move back and forth between different workstations, perceive and map the environment, and transport goods over large distances, for example. Nowadays, both stationary and mobile manipulators are intended to work directly with or in close proximity to human co-workers and shall react compliantly to physical contact. Human safety is, therefore, a primary concern [1]–[5].

Robot safety is a vivid field of research. Many fundamental insights into impact dynamics have been gained from collision experiments and simulations [5]–[9]. Furthermore, many pre- and post-collision schemes have been proposed for fixed-base and mobile manipulators to ensure human safety [8], [10]–[22]. Besides the contact geometry (blunt, edgy, or sharp), the two parameters that have the greatest influence on human injury severity or pain during dynamic collisions are the reflected mass (i.e., the mass perceived upon impact [23]) and the operational velocity [5], [7], [8]. It is important to understand the range of these parameters for a given robot and to relate this data to human injury severity so that effective measures can be taken to ensure safety. In [8], e.g., it was proposed to map the robot reflected mass to a biomechanically safe velocity that can be commanded to the robot. This was done via so-called *safety curves* obtained trough biomechanics impact experiments. Also the current ISO/TS 15066 safety standard for stationary manipulators provides such (model-based) safety curves, which enable robot programmers to plan safe trajectories in shared workspaces. In [24], the concept of safety curves was further developed into the *Safety Map* framework, where the achievable reflected mass and velocity range for the entire robot workspace (or task-dependent subsets) can be related to human injury data. This tool can be utilized for injury analysis and safe robot design already at an early concept phase of the mechanism design and development process.

In robotics literature, safety assessment and impact mitigation mainly considered fixed-base manipulators so far. What is still missing is a systematic analysis of the safety characteristics of mobile manipulators. In this paper, we derive the achievable Cartesian reflected mass and velocity range of two common types of non-holonomic wheeled mobile platforms, i.e., a differential drive and car-like system, and the combination of these platforms with a seven-DOF Franka Emika robot. The qualitative and quantitative effects of the

[1] Technical University of Munich (TUM), Munich Institute of Robotics and Machine Intelligence (MIRMI), Munich, Germany.

[2] Franka Emika GmbH, Munich, Germany.

* The authors contributed equally.

nico.mansfeld@tum.de

[1]Source: Robotnik Automation S.L.L./DARKO project (robot), vecteezy.com (human).
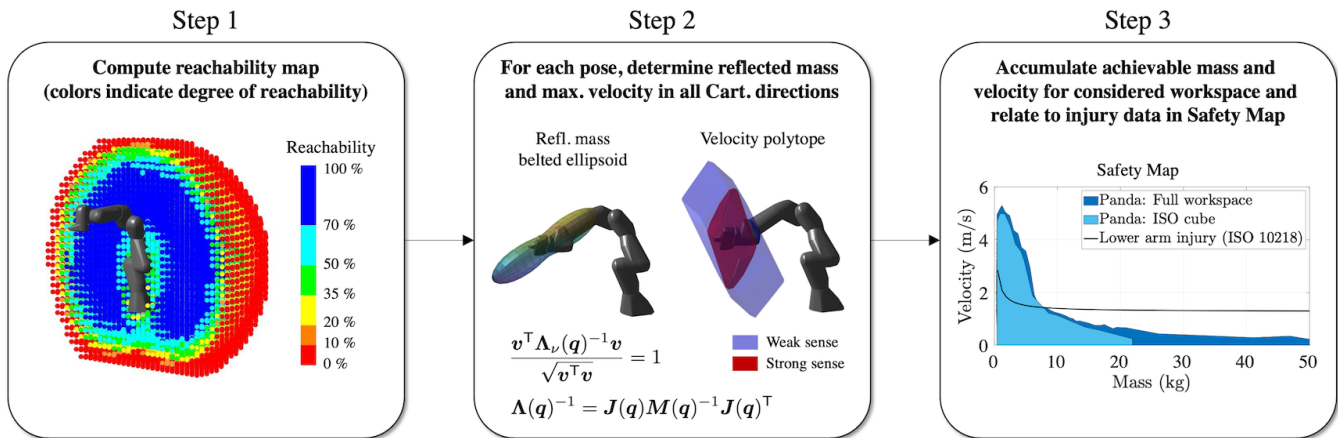
Fig. 2: Derivation of Franka Emika robot's Safety Map representation in three steps. In step 1, the reachability map is computed [25]. For every reachable pose or a task-dependent subset of the workspace, the robot reflected mass (the dynamics provided in [26] were used) and the maximum possible Cartesian velocity are evaluated for a discretized number of Cartesian directions. In the equations, $q \in \mathbb{R}^n$ denotes the generalized coordinates, $M(q) \in \mathbb{R}^{n \times n}$ the mass matrix, $\Lambda_\nu(q)^{-1}$ the upper 3×3 part of the Cartesian mass matrix inverse $\Lambda(q)^{-1} \in \mathbb{R}^{6 \times 6}$, and $J(q) \in \mathbb{R}^{6 \times n}$ the Jacobian matrix at the contact point. The achievable reflected masses and velocities for the entire workspace and the ISO 9283 cube (a subset of the reachable workspace) are accumulated in the Safety Map. Here, the robot's safety properties can be related to injury data, such as the threshold on lower arm injury given in the ISO/DIS 10218 (black line).

platform parameters on the mobile manipulator's collision safety are investigated for different collision scenarios. The mass/velocity data is processed towards the Safety Map, which allows assessing the safety performance of these systems, comparing them to fixed-base manipulators [24], elastic joint robots [27], or other mobile systems. Our results form an algorithmic and data basis to derive future design, planning, and control schemes in the context of safety. Furthermore, the results provide valuable information on the maximum achievable performance in terms of Cartesian endpoint velocity.

This paper is structured as follows. In Sec. II we summarize the Safety Map concept and describe the considered systems and their dynamics. The collision cases and our approach for deriving the achievable reflected mass and endpoint velocity range of mobile manipulators are explained in Sec. III. The results are provided in Sec. IV. Finally, Sec. V concludes the paper.

II. PRELIMINARIES

In this section, we summarize the quantities required to determine the range of reflected mass and velocity and their calculation for fixed-base manipulators. Then, we describe the considered mobile manipulators and their dynamics.

A. Summary of Safety Map for Fixed-Base Manipulators

In the Safety Map, both the robot's safety-relevant properties and human injury data are represented in the mass/velocity plane. The Safety Map representation of a fixed-base robot can be derived in three steps, which are illustrated in Fig. 2 and explained in the following.

Step 1 Determine the reachability map, i.e., the reachable robot poses for a certain discretization of the Cartesian position and robot end-effector orientation [25].

The reachability map of the Franka Emika robot[2] is illustrated in Fig. 2 (left). Positions colored blue are reachable for a high number of end-effector orientations, while yellow/red colored positions have poor reachability.

Step 2 Evaluate the Cartesian reflected mass and maximum possible velocity for every reachable pose or a task-dependent subset of the reachable workspace and a discretized number of Cartesian unit directions via the robot's reflected mass belted ellipsoid [23] and velocity polytope [28]; see Fig. 2 (middle). In the figure, the essential equations for computing the reflected mass belted ellipsoid are provided. The velocity polytope is obtained by transforming the hyperrectangle defined by the maximum and minimum joint velocities $\dot{q}_{\min} \leq \dot{q} \leq \dot{q}_{\max}$ to Cartesian space via $\dot{x} = J(q)\dot{q}$. It can be distinguished between the velocity polytope in the so-called *weak sense*, which considers all translational velocities where the angular velocity may be non-zero, and the *strong sense* polytope, a subset of the weak sense representation that represents purely translational motions [27], [29]; see Fig. 2 (middle, red).

Step 3 Accumulate the achievable reflected masses and velocities for the considered workspace in the Safety Map, where the robot mass/velocity range can be compared to human injury data. In Fig. 2 (right), both the mass/velocity range for the robot's entire workspace and the ISO 9283 cube, a subset of the robot workspace, are illustrated. The figure also depicts the threshold on lower arm injury provided by the current ISO/TS 15066 robot safety standard. It can be observed that in the robot workspace with high reachability (e.g.,

---

[2]The uniform distance between the Cartesian positions is $5\,\mathrm{cm}$. For each position, 20 equally distributed $SO(3)$ end-effector orientations where considered. Both self-collisions and joint position limits were accounted for.

TABLE I: Considered vehicles and their parameters. The drive wheels are shown in black. The location of the manipulator base is indicated by A.

Car-like	Parameters	Differential drive	Parameters
	Wheels (active & passive) Mass: $2\,\text{kg}$ Radius: $0.1\,\text{m}$ Steering angle φ: $\pm 25\,°$ Max. translational velocity: $1.666\,\text{m/s}$ Inertia about axis of rot.: $0.005\,\text{kgm}^2$ **Platform body** Dimensions: $b = 0.6\,\text{m}$ $\quad c = 0.25\,\text{m}$ $\quad d = 0.15\,\text{m}$ $l = 1\,\text{m}$ $\quad h = 0.4\,\text{m}$ Mass: $50\,\text{kg}$ Inertia about center of mass: $5.7\,\text{kgm}^2$		**Active wheels (passive wheels neglected)** Mass: $5\,\text{kg}$ Radius: $0.065\,\text{m}$ Max. translational velocity: $1.666\,\text{m/s}$ Inertia about axis of rot.: $0.006\,\text{kgm}^2$ **Platform body** Dimensions: $b = 0.5\,\text{m}$ $\quad c = 0.25\,\text{m}$ $\quad d = 0.55\,\text{m}$ $l = 0.75\,\text{m}$ $\quad h = 0.393\,\text{m}$ Mass: $124\,\text{kg}$ Inertia about center of mass: $8.94\,\text{kgm}^2$
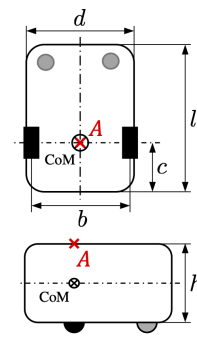
the ISO cube) and relatively low reflected mass, the manipulator can induce injury when it travels at high velocities. Please note that this is only one of many possible (quantitative) insights that one can gain from the Safety Map to assess and optimize robots in terms of safety.

B. Considered Systems and Dynamics

The differential drive and the car-like wheeled platforms that are shown in Tab. I together with their parameters are considered in this work. The drive wheels (black) of the car-like vehicle are coupled and thus rotate at the same speed; the angles of the (also coupled) steering wheels govern the vehicle's steering angle φ. In the differential drive vehicle, the drive wheels rotate independently from each other. Both platforms satisfy the conditions of pure rolling and non-slipping. At the location A on the surface of the vehicles, the seven-DOF Franka Emika robot (total weight of $18\,\text{kg}$) is mounted. The combination of platform and manipulator forms the mobile manipulator.

The kinematic and dynamic equations required to determine the mobile robot's Cartesian velocity and reflected mass are as follows. A detailed explanation of the well-known platform kinematics is omitted for the sake of brevity. For more details, please refer to [30], [31]. The generalized coordinates $\boldsymbol{q} \in \mathbb{R}^{n_v + n_m}$ of a mobile manipulator are composed by the vehicle coordinates $\boldsymbol{q}_v \in \mathbb{R}^{n_v}$ and the manipulator coordinates $\boldsymbol{q}_m \in \mathbb{R}^{n_m}$

$$\boldsymbol{q} = \begin{bmatrix} \boldsymbol{q}_v \\ \boldsymbol{q}_m \end{bmatrix} . \tag{1}$$

In the differential drive, e.g., the Cartesian x/y position and the orientation constitute the position vector $\boldsymbol{q}_v$, while $\boldsymbol{q}_m$ is the vector of the manipulator joint positions. The so-called *steering system* of the vehicle is given by

$$\dot{\boldsymbol{q}}_v = \boldsymbol{S}(\boldsymbol{q}_v)^{\mathbb{S}}\dot{\boldsymbol{q}}_v , \tag{2}$$

where $^{\mathbb{S}}\dot{\boldsymbol{q}}_v$ is the input velocity [30], [31]. For the differential drive, e.g., the input is given by the wheels velocities. The mapping from the input velocity to the differential coordinates $\dot{\boldsymbol{q}}_v$ is given by the constraint auxiliary matrix $\boldsymbol{S}(\boldsymbol{q}_v)$, which includes the vehicle's motion constraints (e.g., on the wheels). The superscript $\mathbb{S}$ indicates the constraint-free space. The velocity vector of the entire system is given by

$$\dot{\boldsymbol{q}} = \boldsymbol{S}_I(\boldsymbol{q})^{\mathbb{S}}\dot{\boldsymbol{q}} = \begin{bmatrix} \boldsymbol{S}(\boldsymbol{q}_v) & \boldsymbol{0} \\ \boldsymbol{0} & \boldsymbol{I} \end{bmatrix} \begin{bmatrix} ^{\mathbb{S}}\dot{\boldsymbol{q}}_v \\ \dot{\boldsymbol{q}}_m \end{bmatrix} , \tag{3}$$

where $\boldsymbol{S}_I(\boldsymbol{q})$ denotes the extended constraint auxiliary matrix. The constraint-free velocities are mapped to operational space via

$$\dot{\boldsymbol{x}} = ^{\mathbb{S}}\boldsymbol{J}(\boldsymbol{q})^{\mathbb{S}}\dot{\boldsymbol{q}} . \tag{4}$$

The Jacobian matrix is given by

$$^{\mathbb{S}}\boldsymbol{J}(\boldsymbol{q}) = \begin{bmatrix} \boldsymbol{J}_v(\boldsymbol{q})\boldsymbol{S}(\boldsymbol{q}_v) & \boldsymbol{J}_m(\boldsymbol{q}) \end{bmatrix} , \tag{5}$$

where $\boldsymbol{J}_v(\boldsymbol{q})$ and $\boldsymbol{J}_m(\boldsymbol{q})$ are the Jacobian matrices associated with the vehicle and the manipulator, respectively. The dynamics of the coupled system can be derived with the macro/mini structure approach proposed in [23]. The kinetic energy of the system is given by $\frac{1}{2}\dot{\boldsymbol{q}}^{\mathsf{T}}\boldsymbol{M}(\boldsymbol{q})\dot{\boldsymbol{q}} = T$, where $\boldsymbol{M}(\boldsymbol{q})$ is the $n_v + n_m \times n_v + n_m$ mass matrix. The mass matrix can be transformed to constraint-free space by inserting (3) into the kinetic energy equation which yields [32]

$$^{\mathbb{S}}\boldsymbol{M}(\boldsymbol{q}) = \boldsymbol{S}_I(\boldsymbol{q}_v)^{\mathsf{T}}\boldsymbol{M}(\boldsymbol{q})\boldsymbol{S}_I(\boldsymbol{q}_v) . \tag{6}$$

After transformation to operational space, we get the 6×6 Cartesian mass matrix inverse

$$^{\mathbb{S}}\boldsymbol{\Lambda}(\boldsymbol{q})^{-1} = ^{\mathbb{S}}\boldsymbol{J}(\boldsymbol{q})\,^{\mathbb{S}}\boldsymbol{M}(\boldsymbol{q})^{-1}\,^{\mathbb{S}}\boldsymbol{J}(\boldsymbol{q})^{\mathsf{T}} . \tag{7}$$

With the upper 3×3 translational part $^{\mathbb{S}}\boldsymbol{\Lambda}_\nu(\boldsymbol{q})^{-1}$ of $^{\mathbb{S}}\boldsymbol{\Lambda}(\boldsymbol{q})^{-1}$ we finally obtain the reflected mass [23]

$$m_u(\boldsymbol{q}) = \left(\boldsymbol{u}^{\mathsf{T}}\,^{\mathbb{S}}\boldsymbol{\Lambda}_\nu(\boldsymbol{q})^{-1}\boldsymbol{u} \right)^{-1} , \tag{8}$$
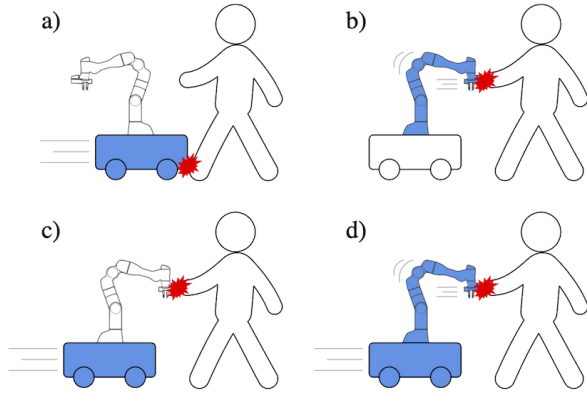
Fig. 3: Possible collision scenarios in the industry. In case a) the platform collides against the human, in b) - d) the manipulator against the human. In a) the platform and potentially also the manipulator moves actively, in b) only the manipulator, in c) only the platform, and in d) both the manipulator and the platform.

of the coupled system in a Cartesian unit direction $u \in \mathbb{R}^3$ while taking the motion constraints of the vehicle into account.

III. Approach

We seek the range of achievable reflected mass (8) and endpoint velocity (4) for the two considered wheeled mobile manipulators. This shall be done for four different industrial collision scenarios we consider important. In this endeavor, we want to analyze the influence of parameters such as steering wheel angle of the car-like platform, the ratio between manipulator and platform mass, or the base velocity on the dynamic properties.

A. Collision Cases

We consider the following four collision cases (see Fig. 3), which are relevant in real-world applications of mobile manipulators:

Case a) When the mobile robot is transporting goods, typically the vehicle is moving while the manipulator is at rest[3]. In this case, the platform may collide against the human, typically at the lower extremities.

Case b) The mobile platform is at rest; the manipulator is moving. This case typically occurs when the mobile robot stops at a workstation and manipulates objects there. For this case, collisions with the upper body are more likely to occur than collisions with the lower body.

Case c) Like a) with the difference that not the vehicle, but the manipulator may collide with the human, typically against the upper body.

Case d) If the vehicle and the manipulator move simultaneously, then the system can exploit its maximum performance in terms of achievable velocity. This can be required to perform explosive motions such as the throwing of objects, for example.

---

[3]In terms of instantaneous collision dynamics, there is no difference between a moving and a resting manipulator in case a).

B. Derivation of the Achievable Mass and Velocity Range

The general procedure for determining the achievable mass and velocity range is the same for all cases a) - d). The different scenarios can be examined by narrowing down the system parameters accordingly. The cases can be distinguished between 1) the contact location(s) and 2) whether the two subsystems vehicle and manipulator are (actively) moving or not. The procedure for deriving the Safety Map representation is as follows.

Step 1 Select the point(s) of interest (POI) on the robot structure. The POI(s) define the contact Jacobian matrix required to determine the reflected mass and the velocity polytope described in the previous section. For our exemplary systems, we consider six POI on the vehicle body (case a)), namely the four corners and the center in the front and back, and one POI at the manipulator end-effector (case b) - d)).

Step 2 Set the velocity constraints. In case a) and c), the manipulator is at rest, i.e., the velocity of every joint is zero. The car-like platform can travel at a velocity within its speed limits; in the differential drive, this holds for both (independent) wheels. In case b) the platform velocity is zero, the achievable Cartesian velocity is governed by the manipulator's velocity polytope described previously. In case d), both the vehicle and the manipulator contribute to the achievable end-point velocity.

Step 3 Sample the robot configurations for the desired parameter range and discretization[4]. For each POI, all combinations of (discretized) platform parameters and the robot's reachability map are determined. In this work, also the ISO 9283 cube is investigated.

Step 4 Evaluate the reflected mass and velocity range for every configuration and in the possible directions of motion. For collisions with the platform, the direction of motion can be constrained by the vehicle's motion constraints. In contrast, the manipulator can typically move in all (discretized) Cartesian directions if the configuration is non-singular.

Step 5 Accumulate the calculated mass/velocity data in the Safety Map and relate the robot representation to injury data and/or other robots' mass/velocity range.

IV. Results

In this section, we provide the results for cases a) - d). For each case, we describe the qualitative and quantitative effects of different robot parameters on the reflected mass and endpoint velocity. The accumulated mass/velocity data is summarized in the Safety Maps illustrated in Fig. 8. There, we also show the current ISO/TS 15066 thresholds for the considered body parts. However, please note that these thresholds only serve as an example. The goal of the paper is

---

[4]The discretization of the robot's workspace and the end-effector orientation is the same as in the previous section. For the car-like vehicle, $\varphi \in [-25, 25]$ ° steering wheel angle with 5 ° increment is selected. For the differential drive, the directions on the unit circle used to evaluate the reflected mass and velocity have 5 ° increment.

(a) Reflected mass and velocity range for $\varphi = 0\,°$ steering angle.

(b) Reflected mass and velocity range for $\varphi = -25\,°$ steering angle.

(c) Reflected mass in the direction of motion over steering angle, $\varphi \in [-40, 40]\,°$.

(d) Maximum velocity in the direction of motion over steering angle, $\varphi \in [-40, 40]\,°$.
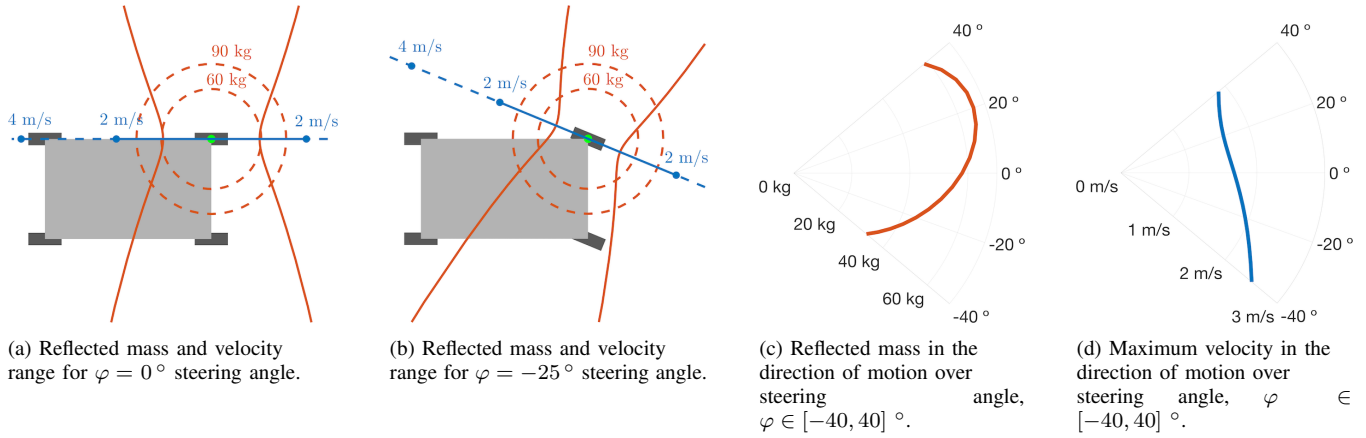
Fig. 4: Polar plots of achievable reflected mass (red) and velocity (blue) for the car-like vehicle at the center of the top right wheel (green circle). In (a) and (b), the reflected mass belted ellipsoid and the achievable velocity range (solid lines) are illustrated for $\varphi = 0\,°$ and $-25\,°$ steering wheel angle. The dashed red circles indicate the magnitude of the reflected mass. In (c) and (d), the reflected mass and maximum velocity at the POI (green circle) in the direction of motion direction are shown for the steering wheel angle range $\varphi \in [-40, 40]\,°$.
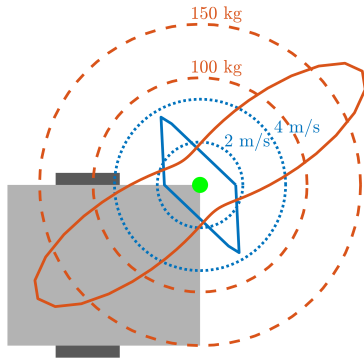
Fig. 5: Achievable reflected mass (red) and velocity (blue) at the top right corner (green circle) of the differential drive vehicle.

to derive the safety-relevant robot dynamic properties, which can be employed for impact mitigation schemes and safety assessment of real-world uses cases in future work.

A. Case a)

In case a), the platform collides against the human, typically at the lower extremities. In the following, we first investigate the achievable mass/velocity range of the two vehicles without attached manipulator, then the effect of the manipulator on the safety characteristics of the coupled system.

1) Vehicle only: For the car-like vehicle, the reflected mass and velocity for a certain steering wheel angle φ and POI are illustrated in Fig. 4 (a) and (b). For $\varphi = 0\,°$, the motion is purely translational, the reflected mass in the direction of motion (along blue line) equals the platform mass including wheels (58 kg). For $\varphi = -25\,°$, the motion has both translational and angular components; the reflected mass is slightly smaller and also governed by the platform inertia. For directions other than the direction of motion, it can be observed that the reflected mass becomes very large (perpendicular to the wheels even infinite), which is due to the vehicle's motion constraints. However, this work

focuses on the reflected mass and velocity range that the robot can achieve in the direction of motion. This analysis is provided in Fig. 4 (c) and (d), where the dependency of both quantities on the steering wheel angle is shown. Results for the differential drive are illustrated in Fig. 5. Those POIs on the platform that are not located on the axis of rotation of the drive wheels can move in every Cartesian direction by variation of the wheel velocities. For rotational motions, POIs close to the wheels typically reach relatively low velocities while the reflected mass is high. Distal POIs (see Fig. 5), on the other hand, can reach high velocities but relatively low reflected mass in the direction of motion. This is also reflected in the Safety Map representations of both systems, which are depicted in Fig. 8 (left column, red area).

2) Combination of Vehicle and Manipulator: Mounting a manipulator on the mobile platform adds extra mass and inertia to the system. The increase in reflected mass can be observed in Fig. 8 (left column, red vs. blue area), the achievable operational velocity remains the same.

B. Case b)

In case b), only the manipulator moves and possibly collides against the human while the vehicle is at rest. The principal influence of the platform parameters (car-like) on the reflected mass of the mobile robot is depicted in Fig. 6. In the figure, the platform steering angle and the platform mass (relative to the manipulator mass) are related to the mobile robot's reflected mass at the end-effector (relative to the stationary manipulator reflected mass). Compared to the fixed-base manipulator, the mobile robot has equal or lower reflected inertia, because the platform adds extra degrees of freedom to the system. The higher the platform mass, the closer the reflected mass of the mobile system gets to the one of the stationary manipulator; see Fig. 6. For $0\,°$ steering angle, the platform's motion direction coincides with the direction considered for reflected mass analysis (x-direction, red arrow). In this case, the additional platform DOF reduce the reflected mass at the end-effector. However,
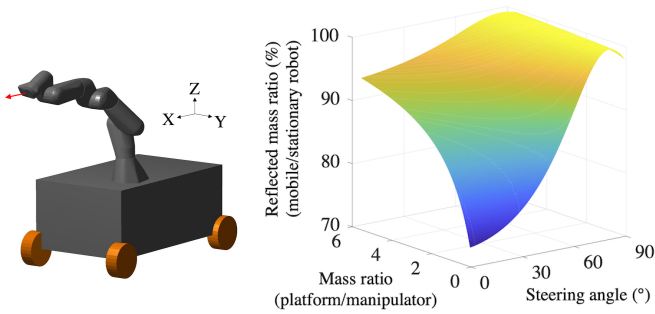
Fig. 6: Car-like mobile manipulator: Influence of the platform mass (relative to manipulator mass) and the platform steering angle on the mobile robot's reflected mass at the end-effector (relative to stationary manipulator reflected mass). The considered near-singular joint configuration is shown on the left, the red arrow indicates the analyzed Cartesian (x-) direction.

the reflected mass increases with increasing steering angle due to the non-holonomic constraints. For $\varphi = 90$ °, the platform blocks the motion in x-direction, which means that the reflected mass of the stationary and mobile robot are equal. The considered manipulator configuration shown in Fig. 6 is near-singular. Because the direction of interest is aligned with several robot links, the reflected mass at the end-effector is comparatively high. As a result, changes in steering angle and platform mass have an influence of up to $30\,\%$ for the considered system. However, in the largest portion of the robot workspace the robot configuration is non-singular. There, the difference in reflected mass between the stationary and mobile manipulator is negligible, which is also reflected in the Safety Map depicted in Fig. 8 (second column). This is because the reflected mass of the Franka Emika robot is mainly governed by the last links, so that the additional platform DOF have only little influence on the reflected mass. This holds for the two considered platforms with 50 and $124\,\mathrm{kg}$ mass, but also for a broader platform mass range; cf. [23]. For simplicity, one can neglect the platform in calculating the reflected mass at the manipulator's end-effector, which is also conservative from a safety point of view.

C. Case c)

In both cases a) and c), only the vehicle is actuated. In case c), however, the manipulator acts as a lever arm during rotational motions (especially in stretched-out configurations), which is why the achievable translational velocity at the end-effector is higher in case c) than the one in case a). In case c), the reflected mass range at the manipulator's end-effector is the same as in case b).

D. Case d)

In case d), both the platform and manipulator are moving. In terms of a potential collision with the manipulator's end-effector, d) is the general case, i.e., the achievable velocity and reflected mass ranges obtained in cases b) and c) are subsets of the one obtained in d). In this case, the maximum possible velocity is comparatively high because the vehicle

and manipulator speed sum up. In Fig. 7, it is shown how the velocity polytope of the stationary manipulator (purple) increases when a mobile platform is added. There, also the influence of the steering wheel of the car-like vehicle becomes visible.

V. CONCLUSION

In robotics injury analysis, it has been shown that the robot Cartesian reflected mass and velocity at the contact location significantly influence human injury severity in dynamic collisions. This is also reflected in the current robot safety standard ISO/TS 15066, which provides a functional mapping between the robot mass and velocity and human pain onset, which can be used for risk analysis and minimization. In this paper, we investigated the achievable reflected mass and velocity range for two mobile manipulators that consist of a wheeled, non-holonomic vehicle and a seven-DOF Franka Emika robot. We analyzed the principal influence of the platform and manipulator parameters on safety and performance properties. The generated mass/velocity data was processed towards the previously introduced Safety Map. Our analysis regarded four different collision scenarios that are relevant in real-world industrial applications. Overall, our approach makes it possible to understand the intrinsic safety characteristics of mobile manipulators and integrate the gained insights and data into future mechanism design and planning methods that enable safe and efficient collaboration between mobile manipulators and human co-workers.

REFERENCES

[1] J. Marvel and R. Bostelman, "Towards mobile manipulator safety standards," 2013, pp. 31–36.

[2] A. Markis, M. Papa, D. Kaselautzke, M. Rathmair, V. Sattinger, and M. Brandstötter, "Safety of mobile robot systems in industrial applications," in *Proceedings of the ARW & OAGM Workshop*, 2019, pp. 26–31.

[3] Robotics Industry Association (RIA), "ANSI/RIA R15.08-1-2020 - American National Standard for Industrial Mobile Robots - Safety Requirements - Part 1: Requirements for the Industrial Mobile Robot," 2020.

(a) Car-like, $\varphi = -40\,°$ (b) Car-like, $\varphi = 0\,°$ (c) Car-like, $\varphi = 40\,°$ (d) Differential drive
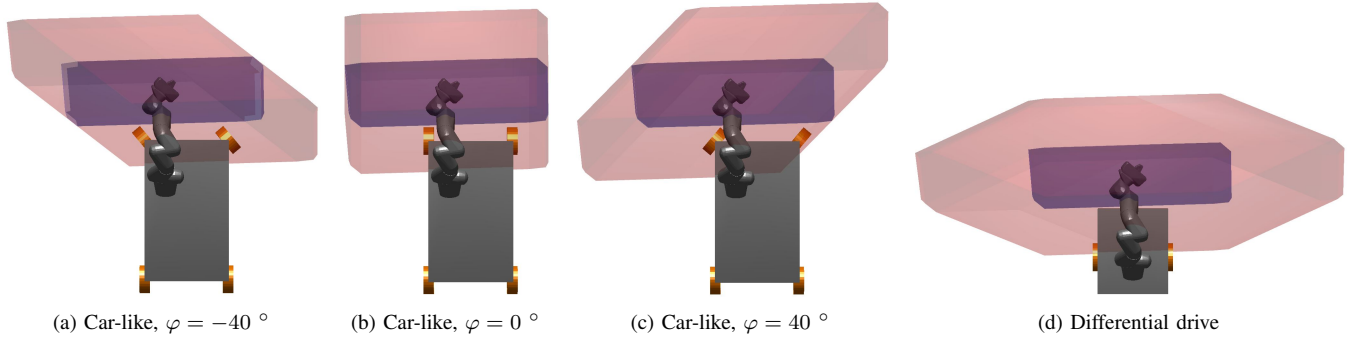
Fig. 7: Cartesian velocity polytope at the end-effector (top view) for two types of mobile manipulators (red) compared to the polytope of the fixed-base manipulator (purple). In (a) - (c), the influence of the steering angle on the velocity polytope is shown for the car-like platform, the differential drive is illustrated in (d).
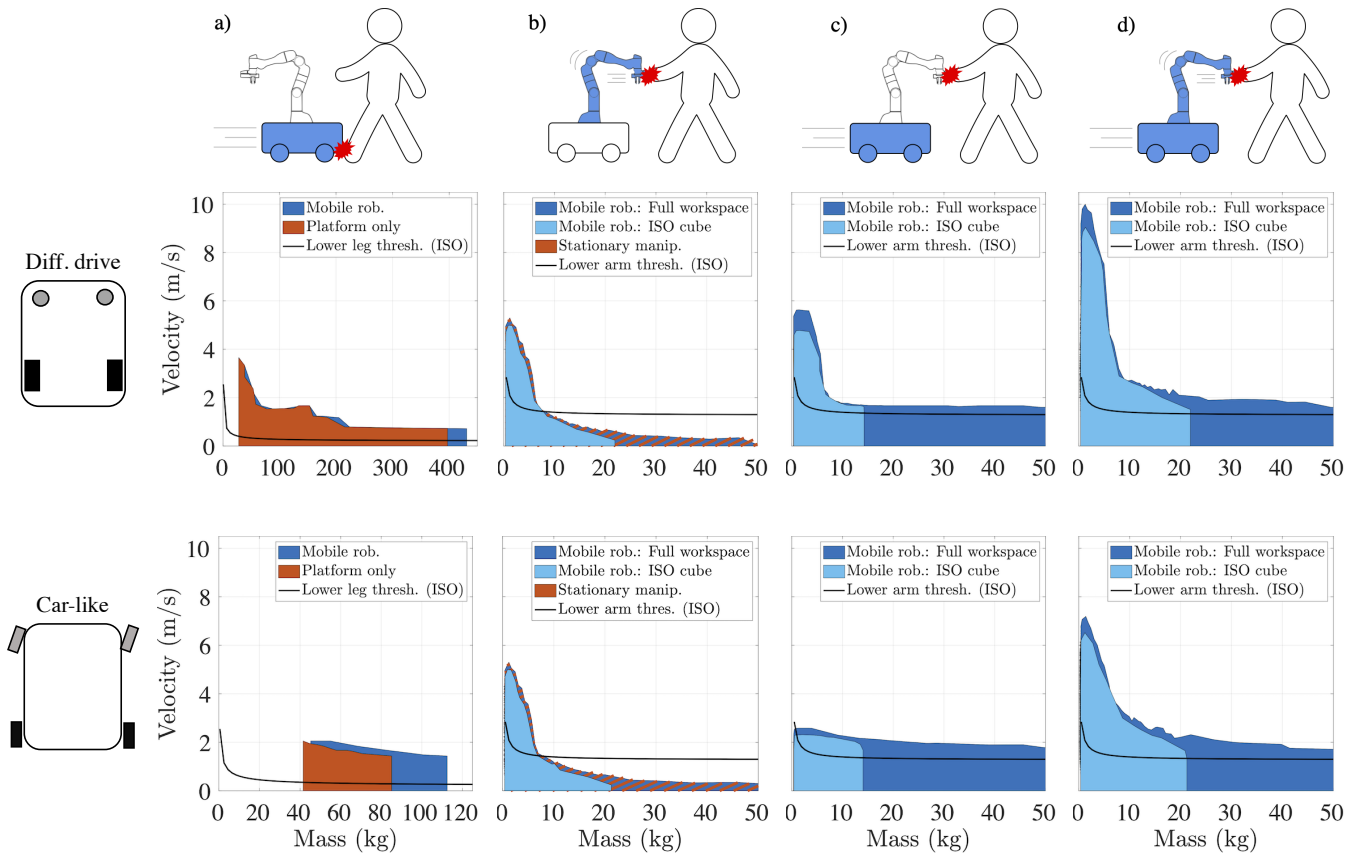
Fig. 8: Safety map representations of two types of mobile platforms including a Franka Emika robot for collision cases a) - d). The dark blue area represents the achievable mass/velocity range of the mobile robot, where the entire workspace of the manipulator is considered. The mass/velocity range for manipulator's ISO cube is illustrated in light blue. For collision case a), the mobile robot (blue) is compared to the platform without attached manipulator (red), for case b), the mass/velocity range of both the mobile robot (blue) and the stationary manipulator without platform (red) are illustrated for comparison. For collisions with the end-effector, the lower arm injury threshold from ISO/TS 15066 is shown, for impacts with the platform the threshold on lower leg injury.

[4] P. Salvini, D. Paez-Granados, and A. Billard, "Safety concerns emerging from robots navigating in crowded pedestrian areas," *International Journal of Social Robotics*, vol. 14, no. 2, pp. 441–462, 2022.

[5] D. Paez-Granados and A. Billard, "Crash test-based assessment of injury risks for adults and children when colliding with personal mobility devices and service robots," *Scientific Reports*, vol. 12, no. 1, pp. 1–12, 2022.

[6] Y. Yamada, Y. Hirasawa, S. Huang, Y. Umetani, and K. Suita, "Human-robot contact in the safeguarding space," *IEEE/ASME Transactions on Mechatronics*, vol. 2, no. 4, pp. 230–236, 1997.

[7] S. Haddadin, A. Albu-Schäffer, and G. Hirzinger, "Requirements for safe robots: Measurements, analysis & new insights," *The International Journal of Robotics Research*, vol. 28, no. 11-12, pp. 1507–1527, 2009.

[8] S. Haddadin, S. Haddadin, A. Khoury, T. Rokahr, S. Parusel, R. Burgkart, A. Bicchi, and A. Albu-Schäffer, "On making robots understand safety: Embedding injury knowledge into control," *The International Journal of Robotics Research*, vol. 31, no. 13, pp. 1578–1602, 2012.

[9] R. Behrens, *Biomechanische Grenzwerte für die sichere Mensch-Roboter-Kollaboration*. Springer, 2019.

[10] S. Haddadin, A. De Luca, and A. Albu-Schäffer, "Robot collisions: A survey on detection, isolation, and identification," *IEEE Transactions on Robotics*, vol. 33, no. 6, pp. 1292–1312, 2017.

[11] A. De Luca and G. Oriolo, "Local incremental planning for nonholonomic mobile robots," in *IEEE International Conference. on Robotics and Automation (ICRA)*, 1994, pp. 104–110.

[12] M. Chen and A. Zalzala, "Safety considerations in the optimisation of paths for mobile robots using genetic algorithms," in *International Conference on Genetic Algorithms in Engineering Systems: Innovations and Applications*, 1995, pp. 299–306.

[13] A. De Luca, G. Oriolo, and M. Vendittelli, "Control of wheeled mobile robots: An experimental overview," *Ramsete*, pp. 181–226, 2001.

[14] V. Padois, J.-Y. Fourquet, and P. Chiron, "Kinematic and dynamic model-based control of wheeled mobile manipulators: A unified framework for reactive approaches," *Robotica*, vol. 25, no. 2, pp. 157–173, 2007.

[15] A. Tuncer and M. Yildirim, "Dynamic path planning of mobile robots with improved genetic algorithm," *Computers & Electrical Engineering*, vol. 38, no. 6, pp. 1564–1572, 2012.

[16] D. Kulic and E. Croft, "Pre-collision strategies for human robot interaction," *Autonomous Robots*, vol. 22, no. 2, pp. 149–164, 2007.

[17] B. Lacevic, P. Rocco, and A. M. Zanchettin, "Safety assessment and control of robotic manipulators using danger field," *IEEE Transactions on Robotics*, vol. 29, no. 5, pp. 1257–1270, 2013.

[18] R. Rossi, M. P. Polverini, A. M. Zanchettin, and P. Rocco, "A pre-collision control strategy for human-robot interaction based on dissipated energy in potential inelastic impacts," in *IEEE/RSJ International Conference. on Intelligent Robots and Systems (IROS)*, 2015, pp. 26–31.

[19] G. Raiola, C. A. Cardenas, T. S. Tadele, T. De Vries, and S. Stramigioli, "Development of a safety-and energy-aware impedance controller for collaborative robots," *IEEE Robotics and Automation Letters (RA-L)*, vol. 3, no. 2, pp. 1237–1244, 2018.

[20] A. Palleschi, M. Hamad, S. Abdolshah, M. Garabini, S. Haddadin, and L. Pallottino, "Fast and safe trajectory planning: Solving the cobot performance/safety trade-off in human-robot shared environments," *IEEE Robotics and Automation Letters (RA-L)*, vol. 6, no. 3, pp. 5445–5452, 2021.

[21] L. Huber, J.-J. Slotine, and A. Billard, "Avoiding dense and dynamic obstacles in enclosed spaces: Application to moving in crowds," *IEEE Transactions on Robotics*, 2022.

[22] J. Haviland, N. Sünderhauf, and P. Corke, "A holistic approach to reactive mobile manipulation," *IEEE Robotics and Automation Letters (RA-L)*, vol. 7, no. 2, pp. 3122–3129, 2022.

[23] O. Khatib, "Inertial properties in robotic manipulation: an object-level framework," *Int. Journal of Robotics Research*, vol. 14, no. 1, pp. 19–36, 1995.

[24] N. Mansfeld, M. Hamad, M. Becker, A. G. Marin, and S. Haddadin, "Safety map: A unified representation for biomechanics impact data and robot instantaneous dynamic properties," *IEEE Robotics and Automation Letters (RA-L)*, vol. 3, no. 3, pp. 1880–1887, 2018.

[25] F. Zacharias, C. Borst, and G. Hirzinger, "Capturing robot workspace structure: representing robot capabilities," *IEEE/RSJ International Conference. on Intelligent Robots and Systems (IROS)*, pp. 3229–3236, Oct.2007.

[26] C. Gaz, M. Cognetti, A. Oliva, P. R. Giordano, and A. D. Luca, "Dynamic identification of the franka emika panda robot with retrieval of feasible parameters using penalty- based optimization," *IEEE Robotics and Automation Letters (RA-L)*, vol. 4, no. 4, pp. 4147–4154, Oct.2019.

[27] N. Mansfeld, M. Keppler, and S. Haddadin, "Speed gain in elastic joint robots: An energy conversion-based approach," *IEEE Robotics and Automation Letters*, vol. 6, no. 3, pp. 4600–4607, 2021.

[28] T. Yoshikawa, "Manipulability of robotic mechanisms," *International Journal of Robotics Research*, vol. 4, no. 2, pp. 3–9, 1985.

[29] P. Chiacchio, Y. Bouffard-Vercelli, and F. Pierrot, "Force polytope and force ellipsoid for redundant manipulators," *Journal of Robotic Systems*, vol. 14, no. 8, pp. 613–620, 1997.

[30] Y. Yamamoto and X. Yun, "Coordinating locomotion and manipulation of a mobile manipulator," in *IEEE Conference. on Decision and Control*, 1992, pp. 2643–2648.

[31] J. Barraquand and J.-C. Latombe, "Nonholonomic multibody mobile robots: Controllability and motion planning in the presence of obstacles," *Algorithmica*, vol. 10, no. 2, pp. 121–155, 1993.

[32] R. Fierro and F. L. Lewis, "Control of a nonholomic mobile robot: Backstepping kinematics into dynamics," *Journal of Robotic Systems*, vol. 14, no. 3, pp. 149–163, 1997.